

Supplemental Information for: Direct-Write Lithiation of Silicon Using a Focused Ion Beam of Li^+

William R. McGehee,^{1,‡} Evgheni Strelcov,^{1, 2,‡} Vladimir P. Oleshko,¹ Christopher Soles,¹ Nikolai B. Zhitenev,¹ and Jabez J. McClelland^{1}*

¹National Institute of Standards and Technology, Gaithersburg, MD 20899, USA

²Maryland NanoCenter, University of Maryland, College Park, MD 20742, USA

I. EELS elemental mapping and quantification

EELS cross sections and energy windows used for elemental mapping are tabulated below. Electron beam energy used for all TEM/STEM imaging is 300 keV. Cross-sections are determined using the Hartree-Slater method.

Table S1: Parameters used for EELS analysis. Electron beam energy is 300 keV.

Transition	Cross-section (barns)	Energy window (eV)	Convergence Semi-angle (mrad)	Collection Semi-angle (mrad)
Li – K	46020	55 to 95	10	13
Si – L	42800	99 to 139	10	13
C – K	2863	283.9 to 323.9	10	32.5
O – K	805	531.9 to 571.9	10	32.5

II. Contamination during Li^+ implantation and TEM imaging

The presence of O and C are also measured using EELS to determine the role of carbon deposition during imaging and reaction with O while under vacuum as well as during the transfer process. Images of n_{Li} , n_{C} , and n_{O} are plotted below for two high ion fluences. The presence of C arises from trace hydrocarbons within the FIB chamber and peaks outside the implanted area.

This result is consistent with ion-implanting-induced deposition, and the C concentration is uncorrelated with the Li concentration, indicating that it is unlikely to have reacted with the implanted Li. Spatial overlap of the O is seen with the Li map indicating that there must be a layer of oxide crust on the spillover Li, which is formed due to gradual oxidation of metallic lithium following deposition.

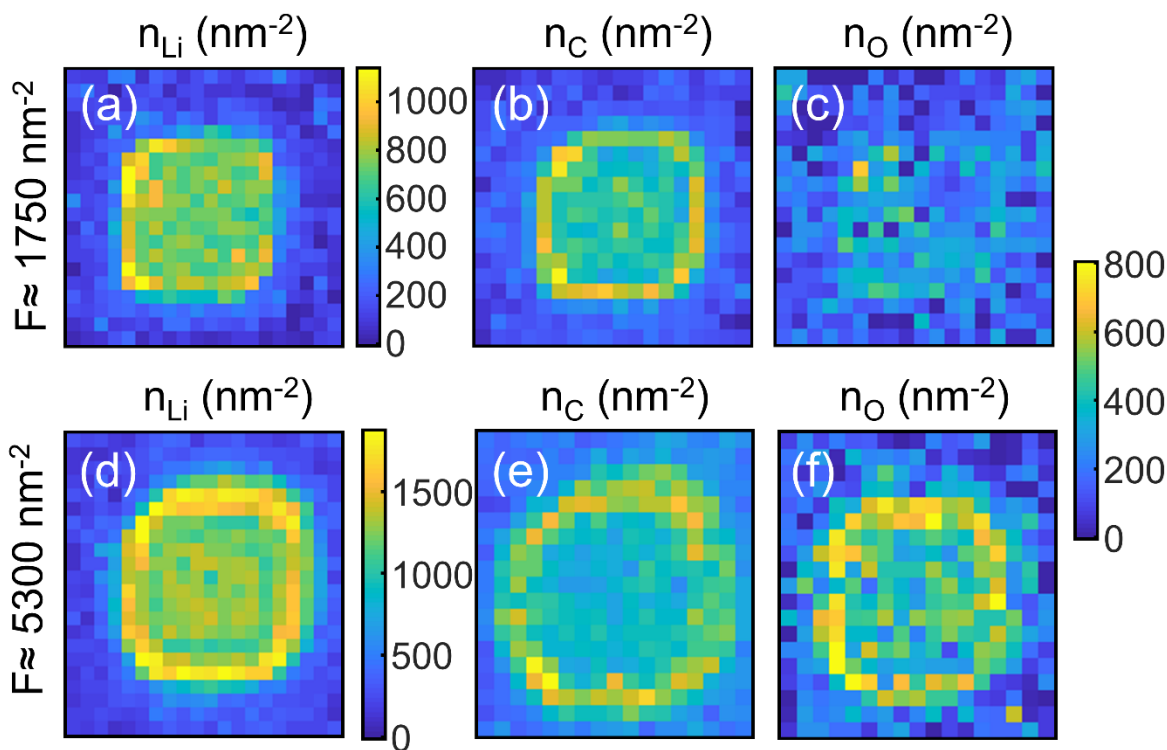


Figure S1 EELS mapping. a)-c) lithium, carbon and oxygen maps, respectively, measured on a Si membrane. The lithiated area was $1\ \mu\text{m} \times 1\ \mu\text{m}$, $F \approx 1750\ \text{nm}^{-2}$. d)-f) lithium, carbon and oxygen maps, respectively, measured on a Si membrane. The lithiated area was $1\ \mu\text{m} \times 1\ \mu\text{m}$, $F \approx 5300\ \text{nm}^{-2}$.

In addition to regular contamination/oxidation, in one instance, the sample was inadvertently exposed to a fluorine-containing material. This occasion helped us determine whether the ion-implanted Li is available to participate in further chemical reactions. The Li-implanted Si membrane was imaged using STEM/EELS on two separate days, and the EELS spectrum from a region was observed to change during the period between the two measurements. We suspect fluorinated vacuum grease (likely originating from an O-ring in the TEM sample holder) contaminated the sample and caused the Li-K line shape to change in a way

consistent with formation of LiF. The two spectra are shown in Figure S2. The initial spectrum (black) is consistent with the data shown in the main text as well as other samples that have been imaged. The spectrum acquired a day later (red) shows a clear modification of the shape of the Li-K line consistent with published values for LiF.¹ While the observed spectrum does not show the delayed edge threshold expected for LiF, this lack is likely a result of its being a combination of the initial Li-K peak shape and the spectrum associated with LiF.

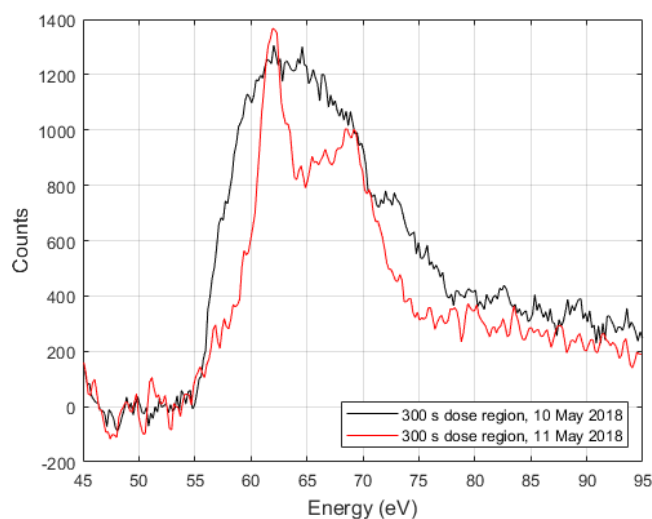


Figure S2. EELS spectrum containing Li K transition taken within several hours of implantation (black curve) and a spectrum taken the next day (red curve). Data are shown after deconvolution and with the background subtracted. Contamination with fluorine-based vacuum grease is likely responsible for the change in the spectrum.

III. Charge dynamics

We hypothesize that the dynamics of Li reduction are controlled in part by local electric fields along the surface of the membrane and by repulsion between charged ions in the membrane—to see this effect, a pair of circular implantation volumes were written close to each other as shown in Figure S3. In one pair the two circular regions were dosed sequentially (one circular region was dosed for 100 s followed by the second for 100 s). The next pair was written in parallel with the ion beam rapidly jumping back-and-forth between the two patterns every 20 ms until both had a total dose time of 50 s. In the patterns written sequentially, spillover mounds form uniformly around the circumference of each region—the same behavior that is observed for a single circular pattern in isolation. In contrast, the patterns written in parallel have spillover in two crescent-shaped regions on the distal ends of the pattern. Self-repelling Li^+ ions in the membrane move as far apart from each other as they can, leaving no mounds formed at the

intersection of the two circular patterns. The switching timescale for the parallel writing provides a lower bound for the reduction time scale in the membrane.

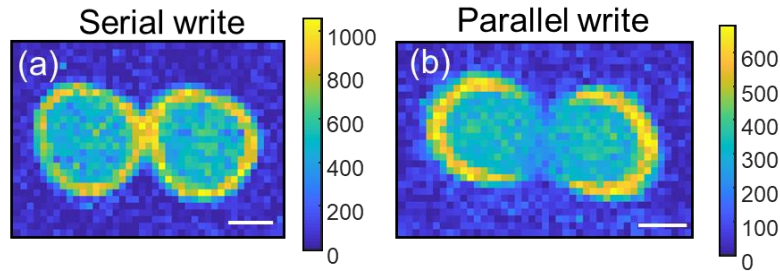


Figure S3. a) lithium map of a lithiated pattern on a Si membrane and consisting of two circular 1 μm diameter areas written in series. b) same, written in parallel. The scale bar is 500 nm.

IV. Cross-sectional view of implantation areas

As stated in the main text, Ga^+ FIB cross-sectioning helps to determine the structure of the lithiated area and surface spillover region. Figure S4a shows an SEM image of a cross-sectioned silicon-on-insulator (SOI) wafer which was lithiated, capped with Pt and milled. The SOI wafer is the same as was used for fabrication of the 35 nm-thick Si membranes. The spillover material and mounds are clearly seen under an e-beam-deposited platinum encapsulating layer, but the thin Si layer underneath is not well resolved. To gain insight into the processes under the Si surface, we lithiated a bulk Si wafer, as shown in Figure S4b-d (same as Fig. 6c-d, main text). Here, we provide more KPFM images in the zoomed-in boxes shown in Fig. S4d to provide a detailed view of the lithiated area and to ensure that the observed CPD distribution is not an artifact of KPFM scanning. Clearly, both trace and retrace (Fig. S4e-h) capture the double CPD band, corresponding to the surface spillover material and bulk lithiated silicon. The zoomed-in view of the “tails” of the cross-sectioned region (Fig. S4i-l) further demonstrate that the on-surface material extends laterally beyond the lithiated area (pink arrow). An SEM image of the AFM tip at the imaged interface is shown in Figure S4m. Note that the radius of the tip curvature is nominally about 25 nm, which is larger than the resolution of the presented KPFM images, implying that a nanoasperity at the tip’s apex must be responsible for the high resolution, as is common for in-vacuum FM-KPFM measurements.

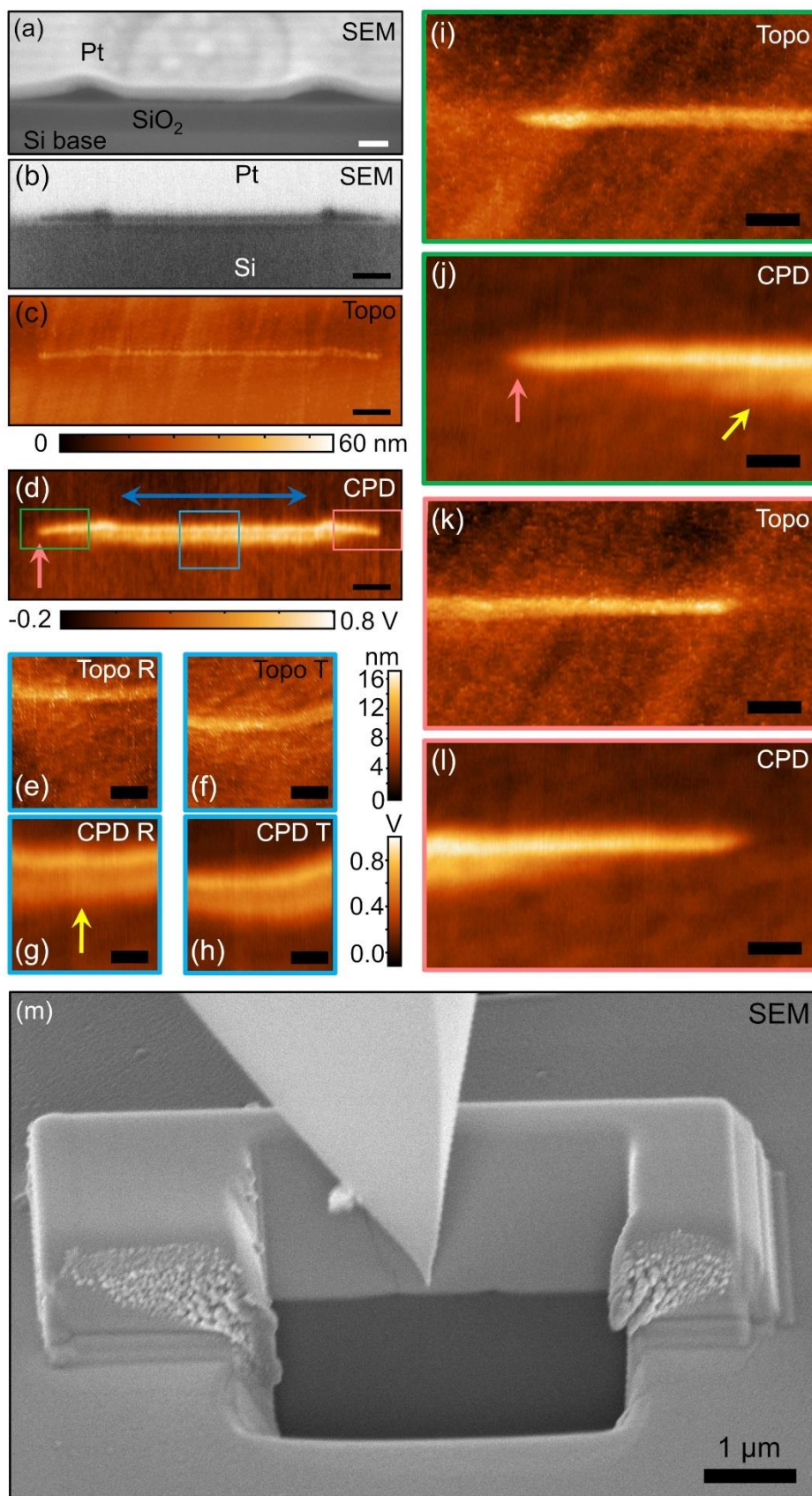


Figure S4. Cross-sectioning the lithiated areas. a) An SEM micrograph of a Ga^+ FIB-milled Li-implantation in an SOI wafer. The implanted area was capped with a Pt layer, seen on top. Below it are dark mounds and a 30 nm thick Si layer followed by the insulating SiO_2 layer and bulk Si base. The fluence for the implantation was $F \approx 1100 \text{ nm}^{-2}$ in $1 \mu\text{m} \times 1 \mu\text{m}$ area. The scale bar is 200 nm. b) An SEM micrograph of a similar cross-section performed on a bulk Si wafer lithiated with $F \approx 1000 \text{ nm}^{-2}$ in a $1 \mu\text{m} \times 1 \mu\text{m}$ area. Besides the dark mounds residing on the surface of Si, a dark band below the Si surface is seen, which corresponds to lithiated silicon. c) and d) Topographic and KPFM maps of the same region as in b). Additional scanning was performed inside the boxed areas and shown in panels (g), (h), (j) and (l) (CPD maps; color scale for all shown in (h)), and (e), (f), (i) and (k) (topographic maps; color scale for (i) and (k) is shown in (f)). For (e)-(h) both trace and retrace images are shown. The wide band of high CPD under the Si surface in the CPD maps (yellow arrows) is clear evidence for lithiation of Si below the spillover mound. Si is lithiated only under the $1 \mu\text{m} \times 1 \mu\text{m}$ implantation area, where the Li^+ FIB was rastered (indicated with blue arrow). The lithiation mound on the surface extends laterally beyond this region, as indicated by the pink arrow. KPFM imaging was performed right after milling, without breaking the vacuum. Scale bars in (a)-(c) are 200 nm; in (e)-(l) – 25 nm. (m) An SEM micrograph of the AFM tip parked in the milled area on the Pt-Si interface. The two mounds appear as dark protrusions into the Pt.

Although the under-the-Si-surface contrast is detected by two techniques with dissimilar contrast formation mechanisms (SEM and KPFM), it is possible that the bands observed in the images appear due to Pt deposition or Ga^+ ion implantation while the sample is cross-sectioned. To test this hypothesis, a bulk Si wafer was FIB-lithiated along a long narrow stripe and then cleaved perpendicular to the implanted stripe in an Ar atmosphere. The exposed, cleaved surface was imaged in SEM (Fig. S5). Despite the absence of Pt and Ga^+ implantation in this sample, a dark narrow band appears in bulk Si right under the lithiated strip. We conclude from this observation that the KPFM and SEM data shown previously are not significantly compromised by the sample cross-sectioning procedure.

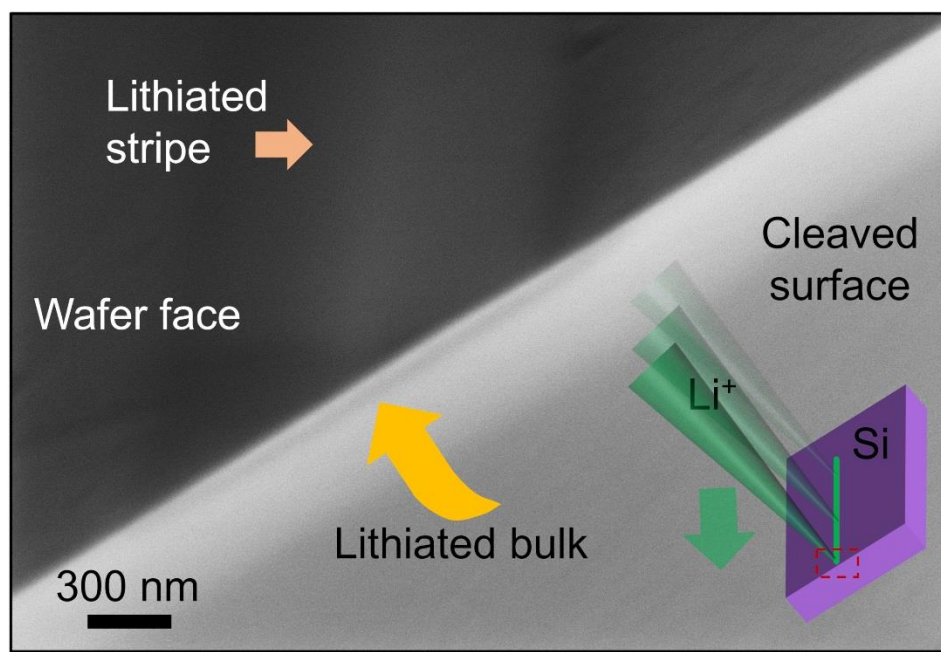


Figure S5. Cleaving a lithiated area. An SEM micrograph of a silicon wafer with a long lithiated stripe written on its face surface as indicated in the inset cartoon and by the orange arrow. Following lithiation, the wafer was cleaved perpendicular to the written line exposing the lithiated bulk (dark band indicated with yellow arrow).

V. Electrochemical activation (delithiation) without spillover

While the main text Figure 7 shows that activation of the injected Li^+ is possible at high lithium doses, when a spill-over region is formed, the question arises, whether same is true for the low-doses, when all the injected Li^+ remains in the Si. It is also important to verify that the material can be de-lithiated. To answer these questions, we have repeated the biased AFM tip experiment (see Fig. 7, main text and surrounding text) at low ion fluence ($F_{\text{Li}} \approx 100 \text{ nm}^{-2}$). At this ion fluence, spillover is not observed, and all implanted Li are expected to remain within the Si. Implantation was performed in a bulk Si wafer followed by AFM imaging, biased AFM scanning, and subsequent AFM imaging as shown in Figure S6. The implanted region (Fig. S6 a,b) has uniform expansion and CPD due to the implantation dose, characteristic of the linear response regime to implantation (no spill-over, or mounds). A halo is evident in the CPD signal surrounding the implanted region, likely due to ion beam instability (and reproduced in perpendicular AFM scanning of the same region). Two small, rectangular regions within the implanted area were scanned with the AFM tip in contact mode and with bias applied to the tip of +10 V and 0 V (Fig. S6a). Following biased scanning, a decrease in CPD of the lithiated area

and accumulation of surface particles are observed as shown in Fig. S6c, d. The rectangular region scanned with 0 V bias shows no change in topography or CPD relative to the regions that were not scanned in contact mode. The rectangular region scanned at +10 V shows a marked decrease in CPD—this is consistent with oxidation of this region and delithiation of the ion mixed $i\text{-Li}_x\text{Si}$ phase. We propose that local delithiation occurred according to: $\text{Li}_x\text{Si} \rightarrow x\text{Li}^+ + \text{Si} + xe^-$. Since no excess Li^+ is observed in the periphery of the implanted region (unlike the example shown in Figure 7, main text), it is assumed that the liberated Li^+ ions migrated deeper into the bulk of the wafer and are not detected by KPFM. These data show that Li^+ in the ion mixed $i\text{-Li}_x\text{Si}$ phase (in the absence of spill-over material) remains electrochemically-active and can be driven spatially by application of suitable potentials.

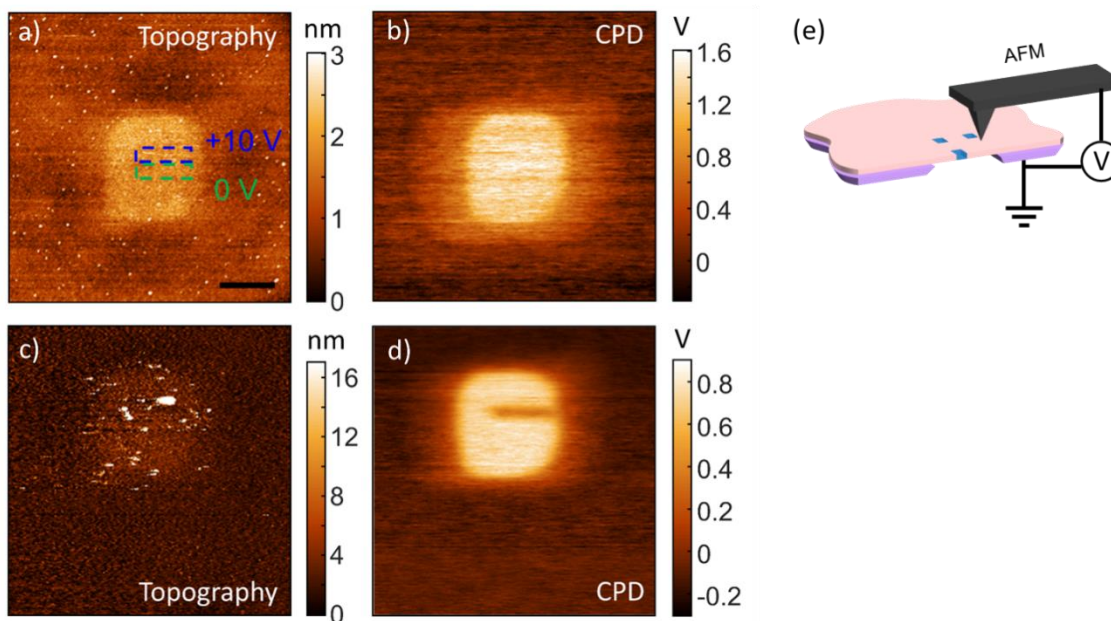


Figure S6. Reactivity of implanted lithium. (a)-(b) Topographic and KPFM images of a lithiated area on Si wafer ($1\mu\text{m} \times 1\mu\text{m}$, $F_{\text{Li}} \approx 100 \text{ nm}^{-2}$). The two dashed $150 \text{ nm} \times 500 \text{ nm}$ boxes indicate regions that were scanned with a +10 V (blue) and 0 V (green) biased AFM tip in contact mode (while sample was grounded). (c)-(d) Topographic and CPD maps of the same area after biased scanning showing oxidation of the 10 V-scanned regions. The scale bars are 500 nm for all panels. The tip's quality has deteriorated due to the reactions run in contact mode, therefore the topographic image of panel (c) looks more noisy than in (a). Accumulation of surface particles is evident in (c), the expansion of the implanted region is otherwise unaffected outside the region scanned at 10 V on. (e) Schematic shows the electrical configuration of biased tip scanning.

VI. Thermal activation

In addition to the voltage bias or e-beam irradiation activation of implanted Li^+ described in the main text, thermal activation can also be used to induce local reactions and ion diffusion. Various transformations can be observed in lithiated annealed Si membranes depending on the Li dose and the imaged side of the membrane. At lower doses, the back (opposite-to-implantation) side of the membrane has a nicely-outlined expansion, corresponding to the implanted area (Fig. S7a) and a matching elevated CPD region (Fig. S7b) After annealing at 700 °C (*i.e.*, at a temperature higher than the melting point of the most refractory bulk lithium silicide phase) in argon, the implanted region and its surroundings develop outgrown nanocrystals, with minimal expansion (Fig. S7c-d). For higher doses, implantation leads to formation of a “blanket layer” area on the membrane side opposite to implantation – an elevated mesa of very high CPD (Fig. S7e-f). Formation of this layer must be related to spillage of the implanted ions onto the back side of the membrane (the surface opposite to the incident FIB). Upon annealing at 700 °C, this layer also develops nanocrystals, but also significantly expands laterally, indicating that the surface diffusion of Li^+ is facilitated relative to the bulk. On the front side of the membrane (facing the FIB), where mounds are grown (Fig. S7i-j), these melt upon heating, deform and expand laterally forming a jagged front (Fig. S7k-l).

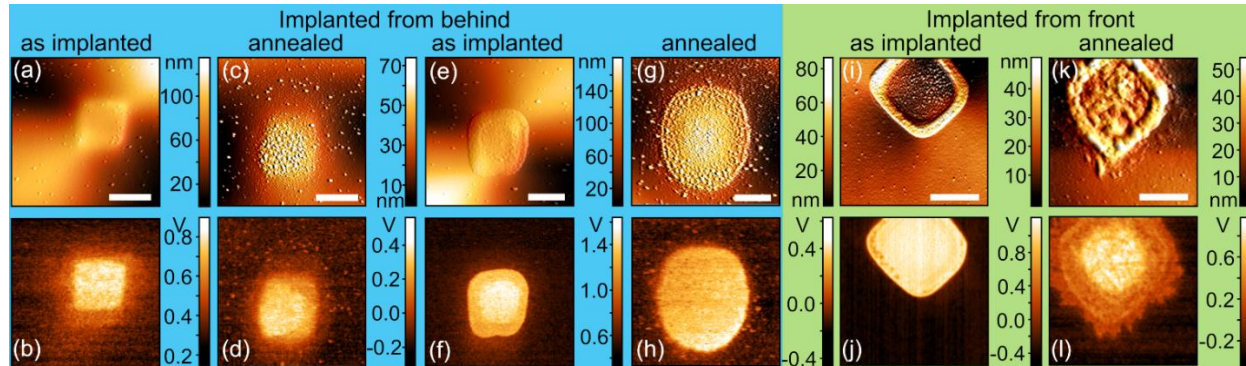


Figure S7. Thermal activation of the lithiated areas. KPFM topographic ((a)-(k), top row) and CPD ((b)-(l), bottom row) images of Si membranes lithiated from the back (blue background) and front (green background), and imaged from the front before and after annealing in an argon-filled glove box. All implanted areas were $1 \mu\text{m} \times 1 \mu\text{m}$. Area shown in (a)-(d) had a fluence of 3400 nm^{-2} and was annealed for 5 min. at 700 °C and 20 min. at 500 °C. Area shown in (e)-(h) had a fluence of 5000 nm^{-2} and was annealed for 5 min. at 700 °C and 20 min. at 500 °C. Area shown in (i)-(l) had a fluence of 950 nm^{-2} and was annealed for 75 min. at 150 °C. Clearly, annealing activated Li^+ diffusion, formation of nanocrystallites and reaction of the mounds with the underlying silicon.

If the dose is high ($> 500 \text{ nm}^{-2}$), and the sample did not have enough time to oxidize, the annealed mounds break into a pattern of interconnected nano-puddles of solidified liquid, which

does not wet the surface well. Figure S8a-b shows AFM topographic images of such a case before and after annealing (at 400 °C in argon), respectively. The same happens on a Ga⁺ FIB milled surface, shown in SEM images of Figure S8c-d. The bulk Si wafer surface was milled flat, but upon annealing, it got flooded with liquid, flowing from under the exposed lithiation mounds. Since these liquid-like patterns appear after annealing at a low temperature, well below the melting point of any known stable lithium silicide (Li₂₂Si₅, m.p. 628 °C), silicon itself (m.p. 1414 °C), platinum (m.p. 1768 °C), lithium oxide (m.p. 1438 °C, hydroxide (m.p. 462 °C), lithium silicate (m.p. 1024 °C), lithium carbonate (m.p. 723 °C). The only known material that could be present in the mounds and has a melting point below 400 °C is metallic lithium (m.p. 181 °C). This fact supports the proposed mound formation model, which assumes build-up of metallic lithium in the mounds.

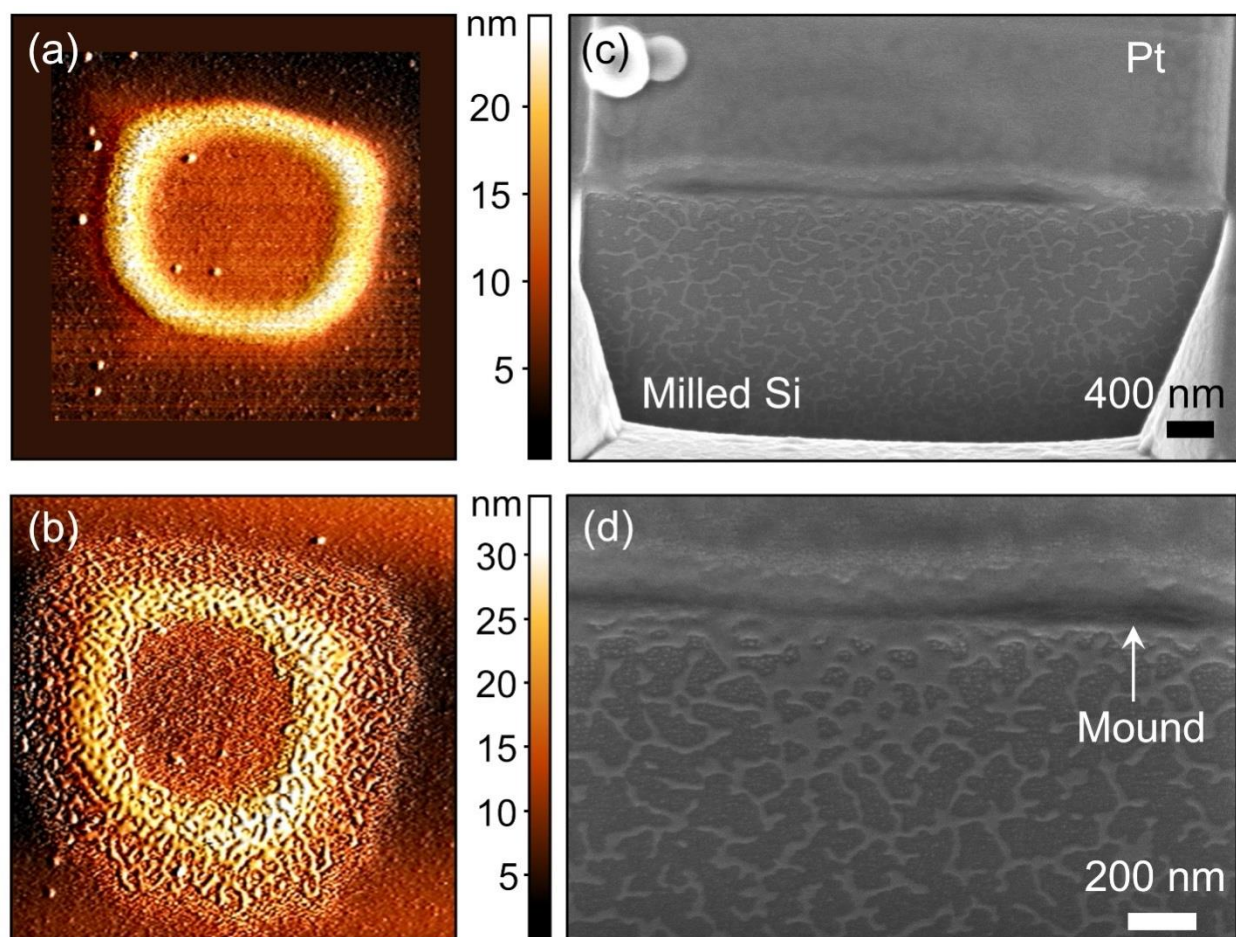


Figure S8. Evidence for metallic Li in the mounds. (a) and (b) topographic images of a 1 μm × 1 μm lithiated area on a bulk SOI wafer ($F \approx 550 \text{ nm}^{-2}$) before and after annealing (at 400 °C for 10 mins., in argon), respectively. Clearly, the mounds partly melted forming a pattern of

interconnected nano-puddles poorly wetting the surface. (c) and (b) are SEM micrographs of a lithiated area ($1\ \mu\text{m} \times 1\ \mu\text{m}$, $F \approx 1900\ \text{nm}^2$) on bulk Si wafer capped with Pt, Ga^+ FIB milled and then annealed at $400\ \text{°C}$ for 15 min. in an argon-filled glove box. The milled Si surface, which was smooth prior to milling, is covered with a network of nano-puddles clearly originating from the lithiated area above it.

VII. Mound-free implantation

The desirable outcome of Li^+ implantation is a uniform distribution of lithium inside the implanted material, without spillage onto the surface and formation of peripheral mounds. Our preliminary tests indicate that this goal can be achieved by cooling down the sample during implantation to suppress diffusion of ions to the surface. Figure S9a-b show KPFM images of a bulk Si area that was implanted while the sample was cooled down to $-80\ \text{°C}$ with a Peltier cooling stage. A clear uniform vertical expansion of the Si in the implanted area is seen, with a matching elevated CPD region, indicative of the absence of bulk-surface lithium segregation. Another route for uniform implantation is using other materials. For example, metallic gold (Fig. S9c-d) shows little topographic changes upon lithiation, and a rich CPD map, indicating Li^+ distribution.

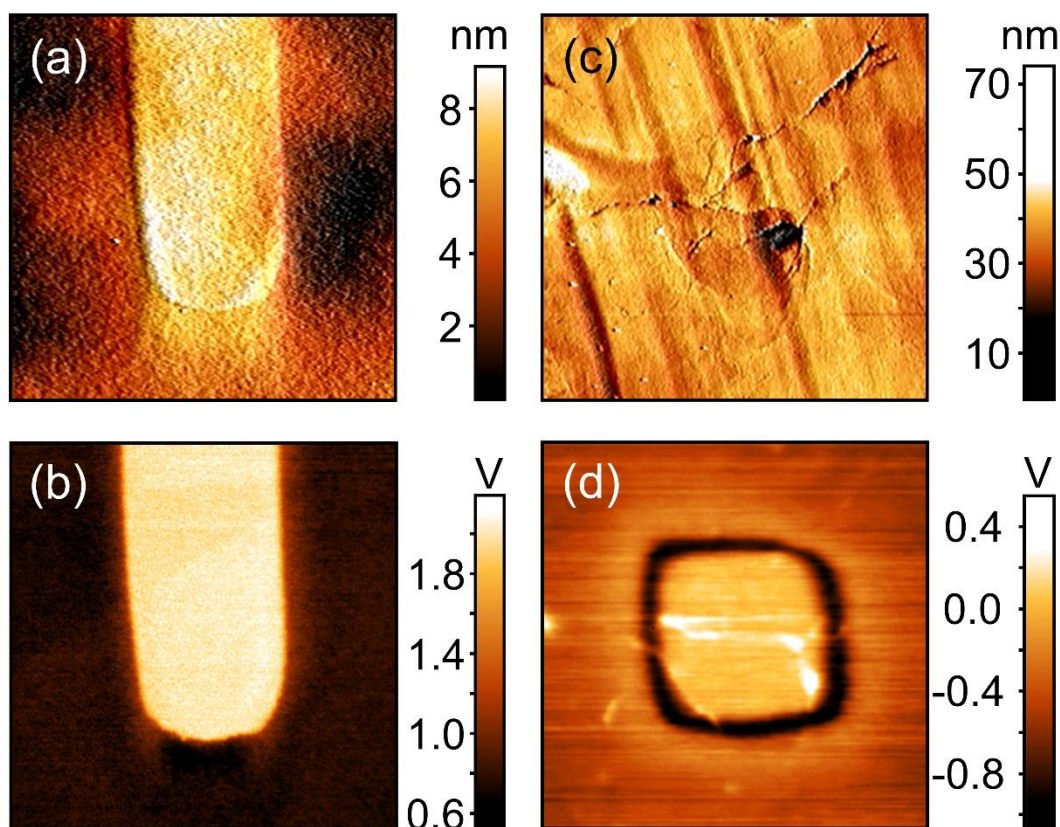


Figure S9. Mound-free implantation. (a)-(b) Topographic and CPD images of a part of the $1\ \mu\text{m} \times 10\ \mu\text{m}$ area, lithiated ($F \approx 560\ \text{nm}^{-2}$) at sample temperature of $-80\ \text{°C}$. The sample is bulk SOI wafer. (c)-(d) Topographic and CPD maps of a $1\ \mu\text{m} \times 1\ \mu\text{m}$ area on gold surface lithiated at room temperature ($F_{\text{Li}} \approx 530\ \text{nm}^{-2}$).

VIII. Selected-area electron diffraction imaging

A selective-area electron diffraction (SAED) pattern from the area A (see Figure 4 in main text) confirms high crystallinity of the diamond type c -Si matrix and reveals barely visible diffuse contours (white arrows) along $[100]$ and $[010]$ directions between the Bragg reflections assigned to ordering of clusters formed by interstitials, which occupy tetrahedral positions in the c -Si crystal lattice.² Because of structural disruption caused by implantation, no diffuse contours are observed in the area B , instead two diffuse rings (large blue arrows in Fig. S10) arise likely due to amorphized metastable Li_xSi . The rings correspond to the most probable interatomic spacings of 0.32 nm and 0.18 nm, which are consistent with a disrupted glass-like Li_xSi alloy coexisting with c -Si and supported by calculations for the tetragonal LiSi ($x=1$) phase performed for the Materials Project.³ For this phase, the calculated major (211) Bragg reflection corresponds to the lattice spacing of 0.337 nm and other two most intensive (312) and (501) diffraction peaks correspond to the spacings of 0.206 nm and 0.177 nm, respectively. The observed broad rings satisfactorily match to these two groups of the LiSi lattice spacings.

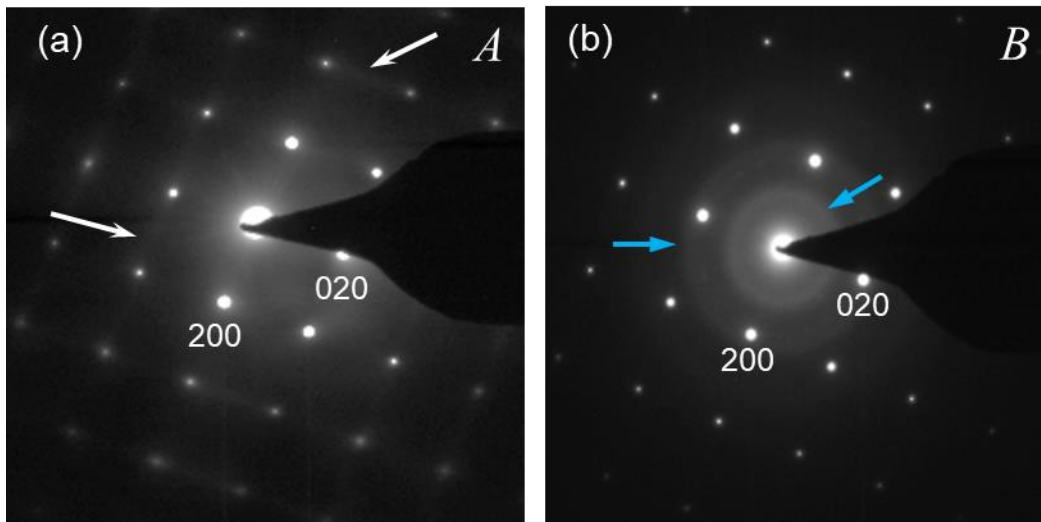


Figure S10. SAED patterns of silicon membrane after implantation. Pristine region A (a) and lithiated region B (b) as in Figure 4 from the main text; zone axis $B = [001]$.

REFERENCES

- (1) Wang, F.; Graetz, J.; Moreno, M. S.; Ma, C.; Wu, L.; Volkov, V.; Zhu, Y. Chemical Distribution and Bonding of Lithium in Intercalated Graphite: Identification with Optimized Electron Energy Loss Spectroscopy. *ACS Nano***2011**, *5*, 1190–1197.
- (2) De Ridder, R.; van Tendeloo, G.; Amelinckx, S. A Cluster Model for the Transition from the Short-Range Order to the Long-Range Order State in F.C.C. Based Binary Systems and Its Study by Means of Electron Diffraction. *Acta Crystallogr. A***1976**, *32*, 216–224.
- (3) Jain, A.; Ong, S. P.; Hautier, G.; Chen, W.; Richards, W. D.; Dacek, S.; Cholia, S.; Gunter, D.; Skinner, D.; Ceder, G.; Persson, K. A. Commentary: The Materials Project: A Materials Genome Approach to Accelerating Materials Innovation. *APL Mater.***2013**, *1*, 011002.